The Importance of Sensor Placement During the Measurement of RF Heating of Implants in MRI

Jenny Wooldridge and Daniel Bownds

Abstract—This study investigates the importance of accurate sensor placement when assessing implant safety during MRI scans experimentally. A combination of measurement and finite element modelling was used to assess sensitivity of measurement to sensor placement, for temperature rises at the ends of a set of calibration cylinders. The simulations used a coupled thermal-electromagnetic model created using COMSOL Multiphysics to replicate the measurement conditions virtually. Thermal gradients in parametric models of cylindrical implants of varying length and diameter were evaluated to quantify the sensor placement accuracy required for the measurement of implant heating within the estimated temperature measurement uncertainty. In this way we aim to enhance the understanding of the requirements for experimental procedures and safety standards dealing with implant heating in MRI.

Index Terms—Magnetic resonance imaging, measurement techniques, finite element methods, implantable biomedical devices, heating.

I. INTRODUCTION

MAGNETIC Resonance Imaging (MRI) is a commonly used medical imagining modality, popular for its high contrast tissue resolution capabilities, and the lack of exposure to ionising radiation. Patients with implanted medical devices are at risk of harm during MRI scans through induced heating of the devices. Whilst safety standards and implant labelling systems are in place, the variability of risk due to the differences in environment (including tissues in which the implant is placed, orientation and location within the scanner, coil size and sequence used) and differences within the implants themselves (for example the implant geometry and materials) result in a unique safety hazard for patients.

The RF electromagnetic fields produced by an MRI transmitter coil induce currents within the implant, resulting in heating via resistive losses. The worst case scenario for RF heating exists within thin, linear implants oriented along the axis of the MRI coil, in which sinusoidal resonant currents can be set up between the ends of the device [1]. The magnitude of this "antenna effect"

is dictated by the electrical properties of the medium in which the implant is placed. The wavelength of an electromagnetic wave propagating in a lossy medium [2] can be written as:

$$\lambda = \frac{2\pi}{\omega \sqrt{\frac{\mu\epsilon}{2} \left(1 + \sqrt{1 + \left(\frac{\sigma}{\omega\epsilon}\right)^2}\right)}}, \tag{1}$$

where ω is the angular frequency, μ the magnetic permeability, σ the electrical conductivity, and ϵ the electrical permittivity. Implants with electrical lengths matching half the wavelength as defined above (equal to 22 cm for a tissue mimicking MR phantom at 1.5 T) will experience the most heating. Resonant conditions of the sinusoidal currents are broken in implants of larger radii and non-cylindrical geometries, resulting in a suppression of the Joule heating. To experimentally investigate this effect, and compare results of implant heating measurements and simulations, a series of steel calibration cylinders of varying lengths and radii were investigated, along with three passive, orthopaedic devices. An assessment of the effect of temperature sensor placement on the accuracy of experimental verification of implant heating is made. With linear implants it should be noted that large temperature rises can occur not just on the implant itself, but also within the tissue or phantom material in which the device is placed, due to a focusing effect of the scattered electric field [3]. The necessity for the accurate placement of temperature sensors during implant safety testing procedures, required to ensure thermal "hot spots" are adequately measured, is an important ongoing problem for experimental validation of MRI heating [4], [5]. Within this paper we employ parametric modelling to quantify the extent of the problem, thereby enhancing the understanding of the requirements for experimental procedures. In addition we perform a review of the published literature containing comparisons of implant heating measurements and simulation results. We report a bias towards lower measurements of heating, consistent with an underestimation of thermal measurement accuracy.

II. METHODS

A. Implant Heating Measurements

Measurements of MRI-induced heating in the steel calibration rods and orthopaedic devices were carried out in compliance with the test method and requirements specified in ASTM

TABLE I
MATERIAL AND GEOMETRY DETAILS OF THE DEVICES
MEASURED IN THIS STUDY

| DUT type	Material	Radius /mm	Length /mm
Calibration Cylinder	Stainless Steel	10	100
Calibration Cylinder	Stainless Steel	3.2	100
Calibration Cylinder	Stainless Steel	1	100
Calibration Cylinder	Stainless Steel	3.2	75
Calibration Cylinder	Stainless Steel	1	75
Calibration Cylinder	Stainless Steel	3.2	50
Calibration Cylinder	Stainless Steel	1	50
Calibration Cylinder	Stainless Steel	3.2	20
Calibration Cylinder	Stainless Steel	1	20
Titan Osteotomy Plate	Ti Alloy		62
Valgus osteotomy plate	Ti Alloy		80
Blount Staple	CrCo		20
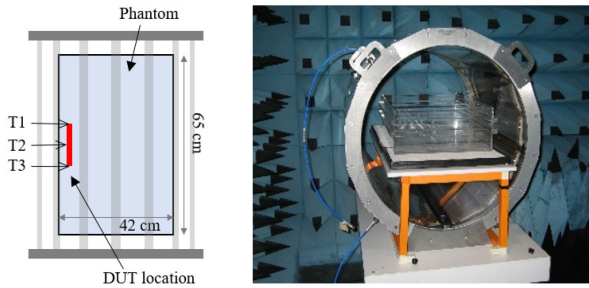
Fig. 1. Left: location of the DUT and phantom in the coil (top view), with the sensor positions T1-3 marked on the image with reference to the cylindrical devices. Right: photograph of the experimental set up.

F2181-11 [6]. A total of nine calibration cylinders were measured, with lengths ranging from 20 mm to 100 mm and diameters in the range from 1 mm to 10 mm. Three sample orthopaedic devices were also investigated, consisting of two different types of osteotomy plate and one surgical staple. Full details of all the test devices are given in Table I. All experimental work was undertaken in an electromagnetically shielded laboratory with RF absorbing material covering the walls and ceiling (a semi-anechoic chamber); the laboratory was temperature controlled to 294 ± 1K. All the equipment used for the measurements was calibrated traceable to primary standards. A Zurich MedTech MITS1.5 64 MHz 16-run high-pass birdcage coil was used to recreate the RF exposure conditions of a 1.5 T MRI scanner [7]. The coil has a length of 650 mm, an inner diameter of 700 mm and the length of the shield is 850 mm. The system was excited in quadrature with a continuous wave signal at the resonant frequency (in the range 63 MHz to 65 MHz).

RF induced heating tests were conducted with the device under test (DUT) submerged in a saline phantom gel with polyacrylic acid (PAA), as specified by [6], within a Plexiglass tank (model ZMI-ASTM2009). The phantom had dimensions of 65 cm × 42 cm × 9 cm and a total mass of 24.4 kg. It was placed with its centroid at the isocentre of the RF coil as shown in Fig. 1. Local heating during a 15 min RF exposure was measured at three positions in very close proximity to the DUT (the locations are indicated in the figure for the cylindrical devices), and one position remote from the DUT, using LuxTron STF or SFF series fast response immersion probes. The tests were then repeated without the DUT to establish the local specific absorption rate

(SAR) at the measurement positions. Sufficient time was left between the tests for the system to return to thermal equilibrium.

The complex permittivity of the phantom gel was measured using a 44 mm coaxial sensor using the methodology set out in [8] and [9]. The sensor, connected to a Vector Network Analyser (VNA) via a phase-stable cable, was calibrated with the reference liquid method using the data published in [10]. Methanol was used as a calibration reference liquid, and a measurement on dimethyl sulphoxide was used to check the accuracy of the calibration. The temperatures of the calibration reference liquids and the sample were measured using a 1 mm platinum resistance thermometer. The samples were viscous and would hold air bubbles, and therefore precautions were taken to exclude bubbles from the measured samples as far as possible. The final measured electrical properties of the gel phantom were 94.4 ± 1.1 for the relative permittivity with a conductivity of 0.50 ± 0.05 S/m^{-1}.

The localised SAR at the temperature probe sites with no DUT present is calculated as:

$$\text{SAR}_\text{L} = c\frac{\Delta T}{\Delta t}, \qquad (2)$$

where c is the specific heat of gel phantom and $\Delta T/\Delta t$ is the gradient of a straight line fitted to the temperature, T, plotted against time, t, using least squares linear regression. With the DUT placed within the phantom, the temperature rise was simply calculated as the difference between T measured at 900 s and immediately before the RF exposure. Where the measured temperature difference was found to be ≤0.2 K, a linear least squares fit was employed to estimate the temperature change, rather than calculating the value from the absolute measurements at 0 s and 900 s. In this way, we minimise the effect of sensor noise on the measurement. The uncertainties on the measurements of local background SAR and the temperature rise on the DUT were estimated as 1.5 W/kg and 0.32 K respectively (based on a standard uncertainty multiplied by a coverage factor $k = 2$, providing a level of confidence of approximately 95%); full uncertainty budgets are provided within the supporting information.

B. Finite Element Modelling

Models of the RF heating induced within the DUTs were carried out using COMSOL Multiphysics v5.6 [11]. The RF induced heating within and around the DUT was modelled using the coupled electromagnetic and heat transfer modules. The propagation of the RF fields generated by the coil is described as

$$\nabla \times \mu_r^{-1}(\nabla \times \boldsymbol{E}) - k_0^2\left(\epsilon_r - \frac{j\sigma}{\omega\epsilon_0}\right)\boldsymbol{E} = 0, \qquad (3)$$

where μ_r is the relative magnetic permeability, k_0 the wave number of free space, ϵ_r the relative permittivity, ϵ_0 the permittivity of free space and ω the angular frequency.

Fourier's law was used to calculate the heat flow within the phantom and DUT

$$m_d c\frac{\partial\vartheta_t}{\partial t} = \nabla \cdot (\kappa\nabla\vartheta_t) + Q, \qquad (4)$$

where κ is the thermal conductivity and Q the heat source.

The MRI apparatus geometry was replicated within the model, with the addition of a sphere of radius 1.75 m containing air surrounding the coil. The coil and shield were modelled as perfect electrical conductors, and the surface of the air sphere was defined as an absorbing boundary to prevent reflections of the RF field back into the coil and phantom. The coil was excited at a frequency of 63.9 MHz, and capacitor elements located at the top and bottom of each rung of the birdcage coil were tuned to achieve the required resonant mode [12]. Given the combination of the high frequency of the excitation and the high conductivity of the DUTs, the skin depth is a negligible fraction of the device size, and so the electromagnetic part of the simulation was not solved within the metallic domain of the DUT, and an impedance boundary condition was defined on the surface of the implant. To perform the finite element simulation, the geometry was meshed with tetrahedral and triangular elements, resulting in meshes with total element counts in the range of 253×10^3 to 369×10^3 for the cylinders and 309×10^3 to 849×10^3 for orthopaedic devices.

Since manufacturer's CAD models for the orthopaedic devices were not available, the implant geometries were measured using an optical scanning probe (Zeiss ViScan). The output files from the scans were found to be too noisy to easily import and mesh, and so dimensions and cross-sectional profiles from the scans were used to draw simplified copies of the devices using the geometry tools available in COMSOL.

To simulate the incident conditions experienced by the DUT during the measurement procedure, technical drawings of the exact location of each cylinder within the phantom were used to set the position of the virtual cylinder within the model. Measurements of local SAR at positions T1 (top centre), T2 (middle, touching at the side) and T3 (bottom centre) without the cylinder present were used to adjust the input voltage on the simulated coil to achieve the measured results; once this calibration was completed the simulation was run once more setting the DUT domain to have the material properties of 304 Stainless Steel (1.4301). Transient simulations were performed with the EM field applied for 900 s followed by 120 s with no field.

III. RESULTS

In the following analysis, the change in temperature between when the field is switched on (at $t = 0$ s) and when the field is switched off (at $t = 900$ s) is reported. Plots of the simulated temperature distributions around the ends of each of the calibration cylinders after 900 s are shown in Fig. 2. The models were post-processed by setting virtual spheres of varying radii (0.1 mm to 12 mm in steps of 0.1 mm) at the centre point on the end of each cylinder, and calculating the maximum and minimum temperatures within the spheres, to mimic an uncertainty in positioning of the temperature sensor during the measurement. The temperature was evaluated on the sphere in both the gel phantom and implant domains. Whilst the placement of the sensor inside the implant is not possible in reality, the uniformity of the temperature within the cylinder (as visible in Fig. 2)
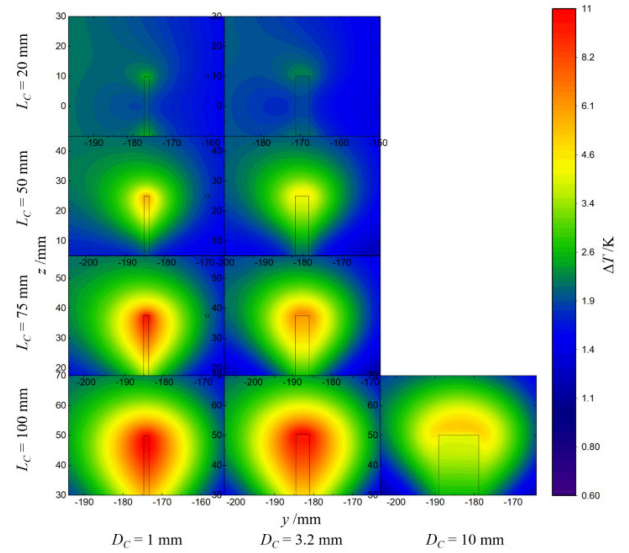

Fig. 2. Simulated temperature profiles around the ends of the steel calibration cylinders. Note the colour axis has been $\ln_2$ scaled in order to visibly differentiate the temperature ranges in each subplot. The subplots are ordered by cylinder length, L_C, and cylinder diameter, D_C.
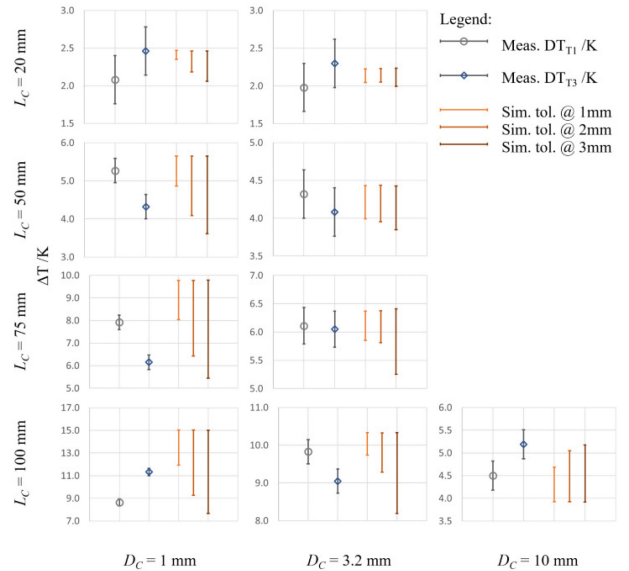

Fig. 3. Measured temperature rises at the top (T1) and bottom (T3) of the steel calibration cylinders plotted as grey circles and blue diamonds respectively, with the estimated uncertainty (k=2) of 0.32 K. Maximum and minimum simulated temperatures within a sphere of radius 1 mm, 2 mm and 3 mm away from the cylinder ends are displayed alongside the measurement values. The subplots are ordered by cylinder length, L_C, and cylinder diameter, D_C.

indicates that the measurement at those internal points would be equivalent to the sensor touching the outside of the implant at the specified distance. The measured values of the temperature rises at the ends of the cylinders (at positions T1 and T3) are shown in Fig. 3 along with results of the post-processing, shown on the right hand side of each of the subplots, for spheres of radii 1 mm, 2 mm and 3 mm. Two thirds of measurements are within the simulation tolerance for the 1 mm radius spheres, with all but one measurement agreeing within a 2 mm radius tolerance,
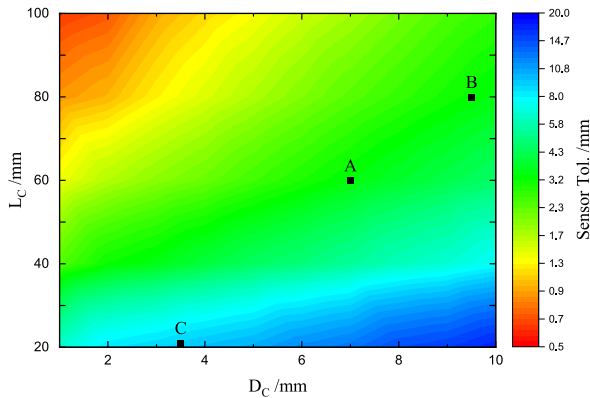
Fig. 4. Required temperature sensor position tolerance to achieve implant heating measurements accurate to within the stated uncertainty of 0.32 K (the colour scale is log transformed). The markers show the approximate dimensions of the three orthopaedic implants depicted in Fig. 5.

and the final measurement (the T1 sensor on the 100 mm long 1 mm diameter cylinder) consistent with a sensor displacement of 2.2 mm from the intended measurement point.

Whilst there is overall a very good agreement between the measurement and simulation results (with a calculated correlation coefficient for the temperature measurements at both ends of the nine cylinders of r(16) =. 95, p<.001.), the observed asymmetry in T1 and T3 measurements suggest that temperature sensor placement is likely to be the limiting factor in the accuracy of the reported results in the case of thin wire implants that give rise to high thermal gradients within the phantom. It is clear from the measurement tolerance values plotted in Fig. 3 that the temperature sensors must be aligned to extremely tight tolerance levels with the DUT (<0.5 mm), at the positions known to give the largest heating values, in order to obtain an accurate measure of the implant heating. In practice this can often be difficult to achieve whilst removing and/or inserting the DUT within the semi-opaque gel of the phantom without disturbing the temperature sensor positions, especially in the case of DUTs with complex geometries.

A series of simulations were carried out for cylinders of lengths L_C in the range of 20 mm to 100 mm and diameters D_C in the range 1 mm to 10 mm. The simulation data were post-processed using the virtual spheres described above and the first derivative of the minimum temperature was calculated to ascertain the thermal gradient as a function of increasing sensor misplacement. Dividing the estimated temperature measurement uncertainty of 0.32 K by the thermal gradient data, we arrive at an estimate of the sensor position tolerance that would be required to achieve implant heating measurements within the stated uncertainties. This estimate, plotted for a range of implant lengths and diameters in Fig. 4, maps out the extent to which it is possible to miss "hot spots" within implant heating safety testing procedures, especially in the cases where adequate modelling has not been performed prior to the measurement procedure, and particularly in the cases of implants which have long, thin wire-like components that are oriented along the length of the MRI coil.

Fig. 5 shows the simulated temperature rises within the three orthopaedic implants, along with the comparison with the experimental measurement results. In this case, all measurements agreed with the simulated data with a temperature sensor location accuracy of 1 mm. These implants have widths that are mostly larger than the cylinders, and therefore we expect a dampening of the antenna effect, resulting in lower amounts of Joule heating within the device. The resultant thermal gradients within the phantom are therefore not significant enough to require a high degree of accuracy in the probe sensor placement. Whilst the complex geometries of the implants cannot be directly compared to the analysis performed on the simplified cylindrical devices, the approximate lateral (calculated as the average of the in-plane sizes) and medial dimensions of the three implants is indicated by the markers in Fig. 4, indicating that the temperature probe positional requirement was approximately 3 mm for the two osteotomy plates and 10 mm for the staple.

IV. DISCUSSION

The results presented above show that there is good agreement between the COMSOL simulations and measurement data for both the steel calibration cylinders and the orthopaedic implants. With the former, large heating values that occur in the longest, smaller diameter cylinders result in high thermal gradients around the ends of the device, requiring sub-millimetre accuracy in temperature sensor placement to correctly measure the largest temperature rise. The effect worsens with increasing implant length, up to the resonant half-wavelength of 22 cm for a implant situated in ASTM gel within a 1.5 T scanner. The measurements and simulations of the orthopaedic devices were found to agree within the closest simulated temperature sensor tolerance of 1 mm; with their larger lateral dimensions there were no highly-localised areas of heating.

A literature review of published works comparing measured and simulated RF heating in implants was carried out; a total of ten publications on implant heating in both wire-like leads and larger orthopaedic devices were obtained (details are provided in Table II). Tabular data and digitised plots of simulated and measured temperature and/or SAR values were extracted from the references giving a total of 294 reported data points. From this information we present the relative errors, defined as the difference between the simulated and measured data normalised by the simulated values, shown in Fig. 6 as a function of implant width. The histogram to the right of the plot clearly shows a bias in the results reported in the literature, towards an underestimation of implant heating obtained from the experimental measurements (positive relative errors). Assuming the models were correctly normalised to the background SAR conditions experienced by the implant, a positive difference between the simulated and measured data could be explained by misplacement of the temperature sensor away from the position of the highest temperature increases produced by the implant. The effect is most clearly observed when looking at the results reported by Stijnman *et al.* [19], shown in Fig. 6 with the black icons. This subset of the data allows us to compare the accuracy of measurements on different implants of three distinct
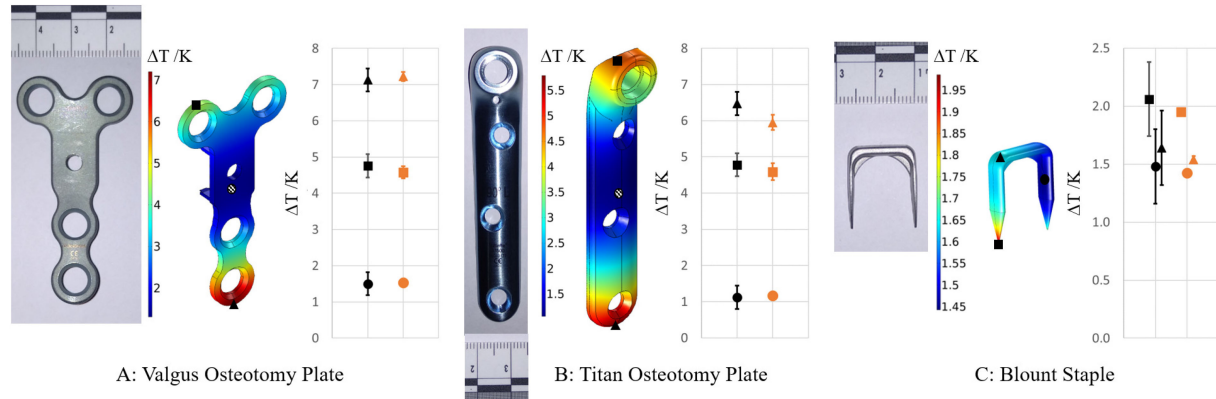
Fig. 5. Photographs of, and simulated heating profiles on, the orthopaedic implants, compared with the measured temperature rises at the three temperature probe locations T1 (black squares), T2 (black circles) and T3 (black triangles). The temperature sensors at position T2 on both the osteotomy plates were located on the back of the implant as shown in the drawings, denoted with a hatched fill icon. The charts show the measured change in temperature (in black, icon shape denotes position on implant) and the simulated temperature rises at the same points measured with a sensor positional accuracy of 1 mm (in orange).

TABLE II
CHARACTERISTICS OF OTHER PUBLISHED WORKS THAT COMPARE SIMULATION AND MEASUREMENT DATA IN RF HEATING EXPERIMENTS, INCLUDING THE SOFTWARE PACKAGE USED WITHIN THE SIMULATIONS, THE TYPE OF IMPLANT STUDIED, THE MEDIUM IN WHICH THE IMPLANT WAS SITUATED, THE WIDTH OF THE IMPLANT AND THE SIZE OF THE STATIC FIELD APPLIED. IN THE MAJORITY OF THE PUBLICATIONS THE MEASURAND REPORTED WAS TEMPERATURE, THOUGH IN SOME CASES DEPOSITED POWER AND SAR (CORRELATES OF THE TEMPERATURE INCREASE) WERE USED INSTEAD

Ref	Figure or Table	Software Used	Implant Type	Medium	Width / mm	B_0 Field / T	Figure 6 icon colour
[13]	Fig. 10 & 11	SEMCAD X	Cardiac lead	ASTM gel	1.5	1.5	Green
[14]	Fig. 5	ANSYS	DBS leads	ASTM gel	1	1.5	Red
[15]	Table 1	Sim4Life	SC stimulator	ASTM gel	6	1.5 & 3	Yellow
[16]	Fig. 2 & 4	ANSYS	DBS leads μMS coil	ASTM gel	0.2 0.4	1.5	Blue
[17]	Table 3	COMSOL	EEG cap	Air	8	3	Light blue
[18]	Table 3	SEMCAD X	Orthopaedic plate	ASTM gel	20	1.5 & 3	Magenta
[19]	Fig. 5	Sim4Life	Bare wire Insulated wire Coax wire SC stimulator	ASTM gel	2.5 2.5 1.25 12	1.5	Black
[20]	Table 2	SEMCAD X	Wire-based sternal closure	ASTM gel	0.8	1.5 & 3	Dark Yellow
[21]	Fig. 9	Sim4Life	Hip prothesis	ASTM gel	30	3	Purple
[22]	Fig. 5	Remcom xFDTD CST Microwave Studio	Dental wire	ASTM gel	1	7	Orange

diameters, tested under the same experimental conditions. An increase in average relative error is observed for the smaller diameter devices, consistent with an increasing difficulty in experimentally locating the maximum temperature increase in these devices.

Within the data reported in this work, we note that the simulated temperature increase is relatively uniform across the width of the ends of the cylindrical implants as shown in Fig. 2. The temperature probe used within our measurements has a lateral dimension of 0.3 mm, and therefore we expect any thermal averaging effect due to the finite size of the temperature probe to only become significant for implants that are narrower than the probe dimensions.

Yao *et al.* [23] presented a method to attempt to overcome the difficulty in locating thermal "hot spots" during implant safety evaluations, by utilising a high-precision robotic measurement system to scan a dosimetric probe at set points around the implant, to produce a map of SAR increase due to the presence

of the implant. SAR was chosen as the measurand rather than temperature, as the movement of the probe within the phantom gel would lead to heat convection effects that would adversely effect the measurement. The measured SAR map is then compared with a high-resolution map of simulated SAR, and least squares regression is used to align the two datasets. From this method, the largest SAR produced within the experiment can be inferred through interpolation, even if the probe missed the point of interest. This methodology neatly combines the use of simulation and measurement for MRI safety evaluations, however it is not yet required by the ASTM standard [6]. The ISO standard [24], whilst technically only applicable to active implanted devices (AIMD), could also be applied, in parts, to passive implants. The measurement process in the ISO standard does describe how to record the spatial distribution of power deposition around hot spots, although the standard also states that power deposition induced by the AIMD can be obtained via magnitude measurements of one or only a few points at or
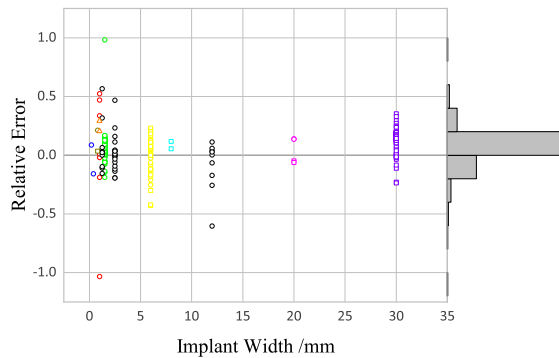
Fig. 6. Measurement error relative to simulation for a variety of thin-wire type implants and orthopaedic devices. Data are reproduced from the references given in Table II; icon colours are also specified in the table. Circles, squares and triangles denote MRI static fields of 1.5 T, 3 T, and 7 T respectively.

around the locations with highest ΔT or SAR, which could lead to an underestimation of implant heating risks.

V. CONCLUSION

Within this work we have validated finite element modelling of implant heating within 1.5 T MRI using COMSOL with experimental measurements. An uncertainty budget was constructed, estimating the uncertainty within the temperature measurements to be 0.32 K (k = 2). A range of calibration cylinders of varying lengths and diameters were measured, resulting in a variety of both maximum temperature rise and spatial thermal gradients around the ends of the cylinders. The simulations were post processed to investigate the effect of temperature sensor placement on the agreement between measurement and simulations. The majority of measurements made agreed with the simulated data for a sensor displacement of 1 mm, with all measurement data covered with a maximum sensor displacement of 2.2 mm. The worst cases of experimental underestimation of the implant heating occurred for the longest and thinnest cylinders that undergo higher levels of Joule heating, and consequently set up higher thermal gradients around the tip.

Three orthopaedic implants were also investigated, with all measurements consistent with a sensor placement tolerance of 1 mm. The larger lateral dimensions of these implants compared with the calibration cylinders results in lower thermal gradients set up within the phantom, and consequently a larger range of sensor position tolerance that is compatible with the stated uncertainty of the temperature measurement. The sensor positional tolerance map produced in Fig. 4 quantifies the experimental requirements for accurate implant heating measurements.

Measurement standards for implant heating validation have minimum requirements for temperature probes to be located at a only handful of points around the DUT. Although the standards specify a minimum required temperature sensor placement accuracy of 0.5 mm (paragraph 8.4.3.5 [24]) or 1 mm (paragraph 8.7.1 [6]), with "accurate and repeatable fixtures", the results presented here suggest that this may be hard to achieve in practice and in certain cases such sensor placement tolerances would not be sufficient. Accurate modelling is essential to assess

the magnitude of thermal gradients expected around the thermal hot-spots prior to experimental evaluation; post-processing of the data of the kind presented in Fig. 4 allows for the experimental set-up requirements to be evaluated ahead of measurements being made. In the cases of implants containing long, thin leads of diameter 2 mm or less, single evaluations of temperature increases may not be enough to prevent under-reporting of the implant heating. In these cases, high-resolution SAR mapping [23] would be a more appropriate evaluation method. However if such methodology is not available to safety test laboratories carrying out experimental evaluations of implant safety in MRI, the results presented in this paper suggest that multiple measurements of the temperature increase should be made, resetting the position of the temperature sensors within the phantom each time to more thoroughly assess the repeatability of the measurement results.

REFERENCES

[1] M. F. Dempsey, B. Condon, and D. M. Hadley, "Investigation of the factors responsible for burns during MRI," *J. Magn. Reson. Imag.*, vol. 13, no. 4, pp. 627–631, 2001. [Online]. Available: https://app.dimensions.ai/details/publication/pub.1048771131

[2] F. T. Ulaby, *Antenna Theory Analysis and Design*, 7th ed. New York, NY, USA: Pearson, 2015, ch. 7.

[3] L. Winter, F. Seifert, L. Zilberti, M. Murbach, and B. Ittermann, "MRI-related heating of implants and devices: A review," *J. Magn. Reson. Imag.*, vol. 53, no. 6, pp. 1646–1665, May 2020. [Online]. Available: https://doi.org/10.1002/jmri.27194

[4] E. Mattei *et al.*, "Temperature and SAR measurement errors in the evaluation of metallic linear structures heating during MRI using fluoroptic probes," *Phys. Med. Biol.*, vol. 52, no. 6, pp. 1633–46, 2007. [Online]. Available: https://app.dimensions.ai/details/publication/pub.1059026989

[5] M. Kozlov and W. Kainz, "Effect of temperature sensor location and measurement time on evaluation of the calibration factor of the lead electromagnetic model," in *Proc. IEEE Int. Symp. Antennas Propag. USNC-URSI Radio Sci. Meeting*, 2019, pp. 765–766. [Online]. Available: https://app.dimensions.ai/details/publication/pub.1122233778

[6] ASTM, "ASTM F2182-19e2, standard test method for measurement of radio frequency induced heating on or near passive implants during magnetic resonance imaging," 2019. [Online]. Available: https://www.astm.org/f2182-19e02.html

[7] Z. M. Tech, "Medical implant test system (MITS) for 1.5 tesla RF safety evaluation," 2021. [Online]. Available: https://zmt.swiss/validation-hw/mits-systems/mits1-5/

[8] A. P. Gregory and R. N. Clarke, "RF and dieletric measurements on layered materials using coaxial sensors," Tech. Rep. NPL Report MAT 13, 2008.

[9] A. P. Gregory and R. N. Clarke, "Dielectric metrology with coaxial sensors," *Meas. Sci. Technol.*, vol. 18, no. 5, 2007, Art. no. 1372. [Online]. Available: https://app.dimensions.ai/details/publication/pub.1034534241

[10] A. P. Gregory and R. N. Clarke, "Tables of the complex permittivity of dielectric reference liquids at frequencies up to 5 GHz," Tech. Rep. NPL Report MAT 23, 2012.

[11] C. M. v. 5.6, "Comsol AB, Stockholm, Sweden," 2020. [Online]. Available: http://www.comsol.com/

[12] G. Giovannetti, L. Landini, M. F. Santarelli, and V. Positano, "A fast and accurate simulator for the design of birdcage coils in MRI," *Magn. Resonan. Mater. Phys., Biol. Med.*, vol. 15, no. 1-3, pp. 36–44, 2002. [Online]. Available: https://app.dimensions.ai/details/publication/pub.1049274437

[13] E. Neufeld, S. Kühn, G. Szekely, and N. Kuster, "Measurement, simulation and uncertainty assessment of implant heating during MRI," *Phys. Med.*

Biol., vol. 54, no. 13, pp. 4151–69, 2009. [Online]. Available: https://app.dimensions.ai/details/publication/pub.1059027684

[14] J. Vu, B. Bhusal, B. T. Nguyen, and L. Golestanirad, "Evaluating accuracy of numerical simulations in predicting heating of wire implants during MRI at 1.5 T," in *Proc. 42nd Annu. Int. Conf. IEEE Eng. Med. Biol. Soc.*, 2020, pp. 6107–6110. [Online]. Available: https://app.dimensions.ai/details/publication/pub.1130399961

[15] A. Yao, E. Zastrow, E. Neufeld, M. Cabanes-Sempere, T. Samaras, and N. Kuster, "Novel test field diversity method for demonstrating magnetic resonance imaging safety of active implantable medical devices," *Phys. Med. Biol.*, vol. 65, no. 7, 2020, Art. no. 075004. [Online]. Available: https://app.dimensions.ai/details/publication/pub.1124806523

[16] G. Bonmassar and P. Serano, "MRI-induced heating of coils for microscopic magnetic stimulation at 1.5 tesla: An initial study," *Front. Hum. Neurosci.*, vol. 14, pp. 1–10, 2020. [Online]. Available: https://app.dimensions.ai/details/publication/pub.1125614387

[17] S. R. Atefi, P. Serano, C. Poulsen, L. M. Angelone, and G. Bonmassar, "Numerical and experimental analysis of radiofrequency-induced heating versus lead conductivity during EEG-MRI at 3 T," *IEEE Trans. Electromagn. Compat.*, vol. 61, no. 3, pp. 852–859, Jun. 2019. [Online]. Available: https://app.dimensions.ai/details/publication/pub.1105109852

[18] Y. Liu, J. Chen, F. G. Shellock, and W. Kainz, "Computational and experimental studies of an orthopedic implant: MRI-related heating at 1.5-T/64-MHz and 3-T/128-MHz," *J. Magn. Reson. Imag.*, vol. 37, no. 2, pp. 491–497, 2013. [Online]. Available: https://app.dimensions.ai/details/publication/pub.1049837803

[19] P. R. S. Stijnman, M. A. Erturk, C. A. T. d. Berg, and A. J. E. Raaijmakers, "A single setup approach for the MRI-based measurement and validation of the transfer function of elongated medical implants," *Magn. Reson. Med.*, vol. 86, no. 5, Nov. 2021, pp. 2751–2765. [Online]. Available: https://onlinelibrary.wiley.com/doi/10.1002/mrm.28840

[20] J. Zheng, M. Xia, W. Kainz, and J. Chen, "Wire-based sternal closure: MRI-related heating at 1.5 T/64 MHz and 3 T/128 MHz based on simulation and experimental phantom study," *Magn. Reson. Med.*, vol. 83, no. 3, pp. 1055–1065, 2020. [Online]. Available: https://app.dimensions.ai/details/publication/pub.1120696615

[21] A. Destruel *et al.*, "A numerical and experimental study of RF shimming in the presence of hip prostheses using adaptive SAR at 3 T," *Magn. Reson. Med.*, vol. 81, no. 6, pp. 3826–3839, 2019. [Online]. Available: https://app.dimensions.ai/details/publication/pub.1112363019

[22] J. Wezel, B. J. Kooij, and A. G. Webb, "Assessing the MR compatibility of dental retainer wires at 7 tesla," *Magn. Reson. Med.*, vol. 72, no. 4, pp. 1191–1198, 2014. [Online]. Available: https://app.dimensions.ai/details/publication/pub.1014537548

[23] A. Yao, E. Zastrow, and N. Kuster, "Data-driven experimental evaluation method for the safety assessment of implants with respect to RF-induced heating during MRI," *Radio Sci.*, vol. 53, no. 6, pp. 700–709, 2018. [Online]. Available: https://app.dimensions.ai/details/publication/pub.1103480265

[24] ISO, "ISO/TS 10974:2018, Assessment of the safety of magnetic resonance imaging for patients with an active implantable medical device," 2018. [Online]. Available: https://www.iso.org/standard/65055.html

Jenny Wooldridge received the M.Phys. degree from the University of Bristol, Bristol, U.K., and the Ph.D. degree in physics in the area of superconductivity and magnetism from Warwick University, Coventry, U.K. She is currently a Senior BI Analyst with National Physical Laboratory (NPL), Teddington, U.K. Since 2019, she has been seconded part time with the Department of Data Science, NPL. In 2008, she joined NPL, where she is working as a Higher, later Senior, Research Scientist within the Materials Division, focusing on the metrology and characterisation of piezoelectric materials. In 2015, she moved into NPL's Strategy directorate and completed a secondment as a Policy Advisor with the U.K.'s Government Office for Science. Dr. Wooldridge is a Member of the Institute of Physics.

Daniel Bownds is currently a Higher Research Scientist with the Electromagnetic Technologies Group, National Physical Laboratory (NPL), Teddington, U.K. In 1999, he joined NPL. He specialises in the magnetic resonance imaging and specific absorption rate areas. He is also a Measurement Services Provider for loop antenna, SAR probe, and monopole calibrations.